Supplementary information

Integrated Theoretical and Experimental Study of Boron Antimonide: Structural, Optical, and Thermoelectric Properties

Kiruthika J[1], S. Nanthini[1,2], Parkavi V[1,3], M. Manjula[4], H. Shankar[2], Lakshmi Prabha Chandrasekar[1,5], Arathyram Ramachandra Kurup Sasikala[6], Suhasini Sathiyamoorthy[7,*], Afeesh Rajan Unnithan[6,*], Pandiyarasan Veluswamy [1,5,*]

[1]SMart and Innovative Laboratory for Energy Devices, Indian Institute of Information Technology Design and Manufacturing, Kancheepuram, Chennai, 600127, Tamilnadu, India

[2]Department of Physics, KPR Institute of Engineering and Technology, Coimbatore, 641407, Tamil Nadu, India

[3]School of Interdisciplinary Design and Innovation, Indian Institute of Information Technology Design and Manufacturing Kancheepuram, Chennai, 600127, Tamilnadu, India

[4]Department of Physics, Sathyabama Institute of Science and Technology, Chennai, 600119, Tamilnadu, India

[5]Department of Electronics and Communication Engineering, Indian Institute of Information Technology Design and Manufacturing Kancheepuram, Chennai, 600127, Tamilnadu, India

[6]Centre for Pharmaceutical Engineering Science, School of Pharmacy and Medical Sciences, Faculty of Life Sciences, University of Bradford, BD7 1P

[7]School of Electronics Engineering, Vellore Institute of Technology, Chennai, 600127, Tamilnadu, India

*Corresponding author
suha.sathiya@gmail.com (Suhasini S),

a.rajanunnithan@bradford.ac.uk (Afeesh RU),

pandiyarasan@yahoo.co.in (Pandiyarasan V)

Text summary:

This study develops a chemical method to synthesize boron antimonide (BSb) for the first time, integrating experimental and theoretical approaches to investigate its structural, optical, electrical, and thermal transport properties, providing comprehensive insights into its thermoelectric characteristics.

1. Synthesis

Initially, 20 ml of 0.5 M $NaBH_4$ solution dissolved in deionized water was stirred at 300 - 400 rpm. Then 20 ml of 0.5 M $SbCl_3$ solution dissolved in deionized water and 10 ml of Con.HCl was stirred for 10-15 minutes till a clear solution was obtained. When $SbCl_3$ is added to water, it undergoes rapid hydrolysis, forming a white precipitate (SbOCl) that hinders further reaction. To prevent this, concentrated HCl is added to suppress hydrolysis, a common reaction where water breaks chemical bonds. The $NaBH_4$ solution was added dropwise to the $SbCl_3$ solution in an ice bath within an exhaust closet. This slow addition in a cold environment is crucial to control the violent and exothermic reaction between $NaBH_4$ and metal halides. A black precipitate was formed upon the complete addition of $NaBH_4$. After 1 hour, the obtained mixture was transferred to a Teflon-lined autoclave and kept in the oven at 423 K for 12 hours. Once the autoclave was cooled to room temperature, the sample was washed with deionized water to remove the soluble impurities such as undissolved ions, and the remaining precipitate was allowed to dry at 343 K for 6 hours. The dried sample was then kept in the tubular furnace for sintering at 773 K for 3 hours in an argon atmosphere to prevent oxidation and unwanted contamination like water vapour. Sintering at high temperature helps to densify the material, promotes grain growth, induces phase transformations, and improves crystallinity. Finally, the obtained sample was finely powdered and used for further characterization. The obtained BSb powders of different ratios were synthesized in the same manner and then made into circular pellets using the cold hydraulic press at 5-6 torr pressure for Hall effect and Seebeck measurements. The synthesis was done with three different molar ratios 1:1, 1:2, and 2:1 of boron and antimony sources namely S1, S2 and S3 respectively.

2. Characterization

The prepared sample is studied under X-ray diffraction (XRD) analysis using a Bruker D8 advanced powder XRD instrument, utilizing Cu K-α radiation (λ = 1.5418 Å) at 40 kV and 30 mA. Data were collected incrementally at 0.02-degree intervals with a step duration of 0.3 seconds. Morphological examination of the BSb material was performed via scanning electron

microscopy (SEM) operating in high vacuum mode at ×500 magnification. Fourier-transform infrared (FTIR) spectra were obtained from powder samples within the wavelength range of 400 - 4000 nm using attenuated total reflectance (ATR) mode to study about their chemical bonds and functional groups. Optical bandgap assessment was conducted via UV-visible spectroscopy utilizing a UV 3600 PLUS series instrument within the range of 200 to 800 nm. Concurrently, Hall effect measurements were performed on cylindrical pellets (13 mm diameter, 1 mm thickness) at room temperature (~303 K). These measurements included resistivity (ρ), Hall coefficient (Rh), carrier concentration (n), mobility (μ), and semiconductor type. The Vander Pauw method, a four-probe technique with low contact resistance, was employed to determine the average resistivity of the samples[1].

The Seebeck coefficient of the material was determined using a homemade measurement system under vacuum conditions at room temperature. A differential two-probe method was employed to continuously record voltage and temperature differences across the sample. The linear relationship between ΔV and ΔT was used to calculate the Seebeck coefficient, an intrinsic property linked to the electronic structure of material. This method is independent of the sample geometric configuration[2].

$$\alpha_{AB} = \Delta V / \Delta T \qquad (1)$$

where α_{AB} is the Seebeck coefficient, ΔV is the voltage difference and ΔT is the temperature difference.

Thermal conductivity and thermal effusivity are essential thermal properties that characterize the heat transfer behavior of material. Thermal conductivity quantifies a material's ability to conduct heat, while thermal effusivity measures its capacity to exchange heat with its environment. In this study, thermal conductivity was determined using the relation $K = e^2 / (\rho C_p)$, where e is the thermal effusivity, ρ is the density, and C_p is the specific heat capacity. Thermal conductivity (κ) and thermal effusivity (α) were measured using a Trident MTPS Sensor from C-therm Instrument over a temperature range of ambient to 353 K.

3. SEM analysis

The morphology of BSb material was examined using a scanning electron microscope (SEM) at two different scale magnifications shown in Fig. SP 1 (a & b), illustrating the surface morphology of the BSb sample S1. At the microscale level, the BSb nanoparticles of S1 show a uniform distribution of particles within the range of 30-200 μm across the surface.

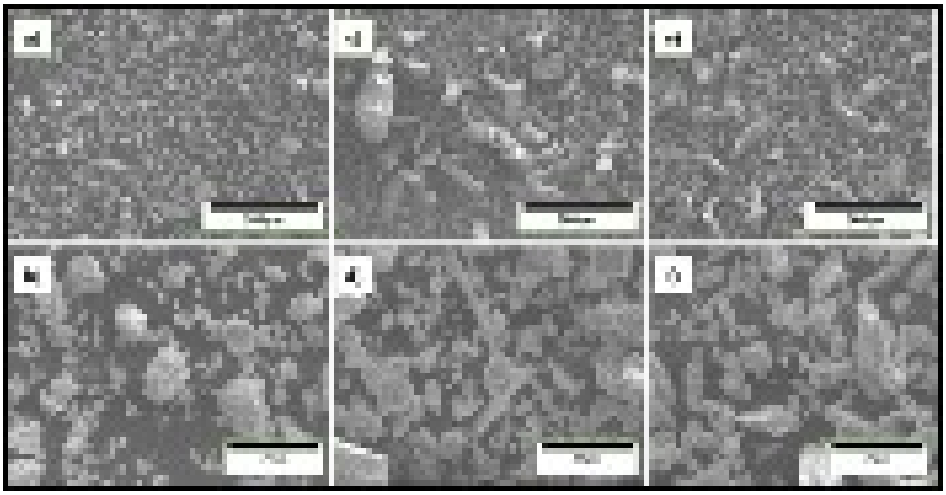

Fig. SP 1 Morphological analysis of BSb through SEM images for samples S1 (a, b), S2 (c, d), and S3 (e, f).

The observation at 30μm reveals that the particles exhibit rigid, irregularly shaped globular nanostructures. In S1, the nucleation process likely leads to the formation of these small, uniformly distributed particles due to the balanced ratio of boron and antimony, which promotes even nucleation and growth. In S2 (Fig. SP 1 c & d), there is a mix of small particles and larger rod-like structures, indicating an increase in particle size compared to S1. Similarly, S3 (Fig. SP 1 e & f) shows a mix of particle sizes with prominent rod-like structures. The variation in the constituent elements in S2 and S3 can lead growth kinetics towards the excess in one element ratio that promotes the formation of higher, rod-like structures due to anisotropic growth, where the growth rate varies in different crystallographic directions. These structures aggregate into bulk forms while maintaining a homogeneous dispersion throughout the sample matrix.

In the SEM analysis, the increase in particle size with a higher molar ratio of elements can be explained by Ostwald ripening. At higher concentrations, many smaller particles are initially formed, creating a larger surface area. This allows larger particles to grow by absorbing material from smaller, unstable particles, which dissolve and release their material. This process reduces the number of particles but increases their size, which lowers the overall surface energy. In samples S2 and S3, this morphology likely strengthens the grain boundaries, which can improve the Seebeck coefficient and lattice thermal conductivity by enhancing phonon scattering.

4. Optical properties

The band structure calculation was compared and analyzed with the UV-visible absorption spectra of the prepared BSb powders, measured using a UV-3600 Plus Series

$$(\alpha h\upsilon)^n = A(h\upsilon - E_g) \quad (2)$$

spectrometer between 200 and 800 nm. The band gap of BSb was estimated by Tauc plots, using the equation (2), where α, h, ν, A, and E_g are the Absorption coefficient, Plank's constant, Photon frequency, proportionality constant, and Bandgap energy. Depending on whether the transition is direct or indirect, n can be 1/2 or 2. As the linearity was considered as 1/2, a tauc plot between $(\alpha h\nu)^{1/2}$ and eV was constructed by extrapolating the linear portion of the curve graph to find bandgap. For materials possessing a direct bandgap, the exponent "n" assumes a value of 2, while for those with an indirect bandgap, it takes on a value of 1/2. By extrapolating the linear absorption edge segment of the $(\alpha h\nu)^2$ versus hν graph, where "hν" denotes energy in electron volts (eV), the optical bandgap energy of BSb can be determined.

5. FTIR spectroscopy

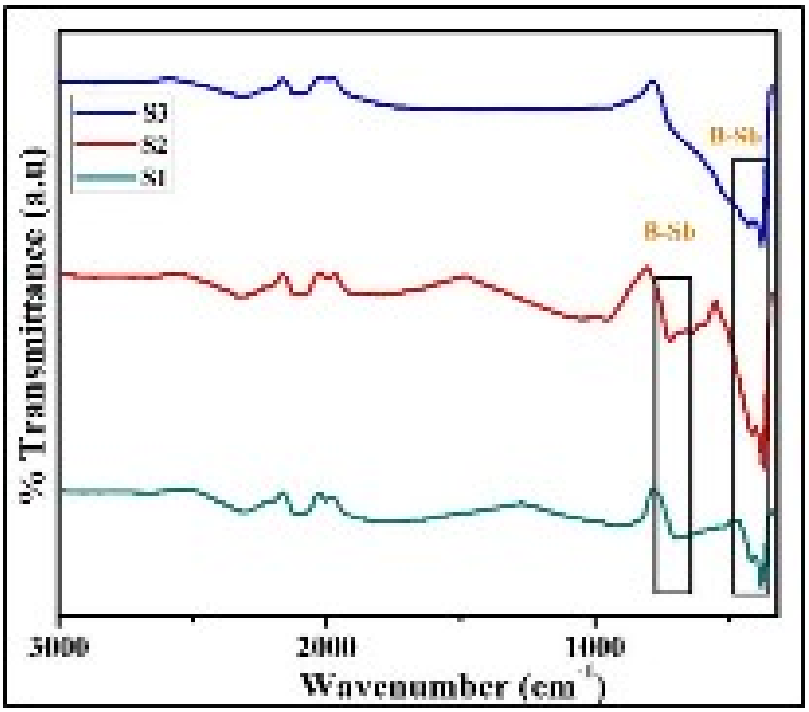

Fig. SP 2 FTIR spectrum of BSb obtained through chemical synthesis.

Fourier Transform Infrared Spectroscopy (FTIR) was used for characterizing the molecular vibrations of various compounds and to study about their chemical bonds and

functional groups. The BSb sample exhibits B-Sb bonds in the 370-380 cm^{-1} and 690-705 cm^{-1} wavelength ranges. In the spectra shown in Fig. SP 2, a prominent band with strong intensity observed within the 370-390 cm^{-1} range is consistent across all samples with varying molar ratios, indicating characteristic infrared absorption band of BSb. This intense band may be attributed to reduced energy absorption by electrons, which could lead to rotational transitions within the far IR region. However, traditional rotational vibrations do not occur in material due to the constraints of the crystal lattice. Instead, the observed band is more likely related to more complex vibrational modes described by phonons, which reflect the collective atomic motions within the solid structure[3]. The moderate intensity band observed in the 680-690 cm^{-1} range corresponds to the stretching vibration of the B-Sb bond in the BSb sample. This band is likely associated with the intrinsic lattice vibrations of the BSb structure and previously reported experimental data from pulsed laser deposition and theoretical studies[4]. In S2 and S3, the excess in the one element ratios affected the vibrational modes, resulting in slight distortions or variations in the lattice that led to minor broadening of the band in our obtained spectrum. However, the fundamental vibrations of B-Sb bonds remained dominant, as indicated by the prominent band in the spectra. S. Das et.al reported that the vibrational modes centered around ~1124 cm^{-1} suggest B–B stretching, while modes in the 1000-1500 cm^{-1} range are associated with B–C bonds, and Sb–O bonds are identified around 750 cm^{-1} [4]. However, in our analysis of the BSb powder spectrum, there is no evidence of B–C or B–B bonds, nor any indication of oxide bonds such as B–O or Sb–O. The absence of B-O or Sb-O may be due to low oxide content and potential overlap with other spectral features[5]. The bonding in BSb is thus characterized by a combination of weak covalent and ionic interactions, providing stability and flexibility to the lattice structure, as evidenced by the consistent vibrational modes and charge density analysis.

6. Hall measurement

Resistivity and Hall measurements were conducted on BSb samples at room temperature. Consistent with the wide bandgap observed in optical studies, surface conductivity was notably low. Hall measurements were performed using an input current source 1 A (ampere). The resulting data facilitated the determination of resistivity, conductivity, carrier concentration, and carrier type for each sample. Fig. SP 3 from (a - d) shows the variation of electrical conductivity, resistivity, mobility and carrier concentration of sample code S1, S2 and S3. Resistivity and hall measurement tests were performed on each sample of BSb at room temperature and the measured values are given in Table 1. The

conductivity values for S1 and S2 are comparable with S2 exhibiting the lowest value (6.52×10^{-3} Sm^{-1}). This may be due to the reason that if the molar concentration deviates from this pristine ratio S1, it can create defects in the crystal lattice. These defects act as scattering centers for electrons, hindering their movement and reducing electrical conductivity.

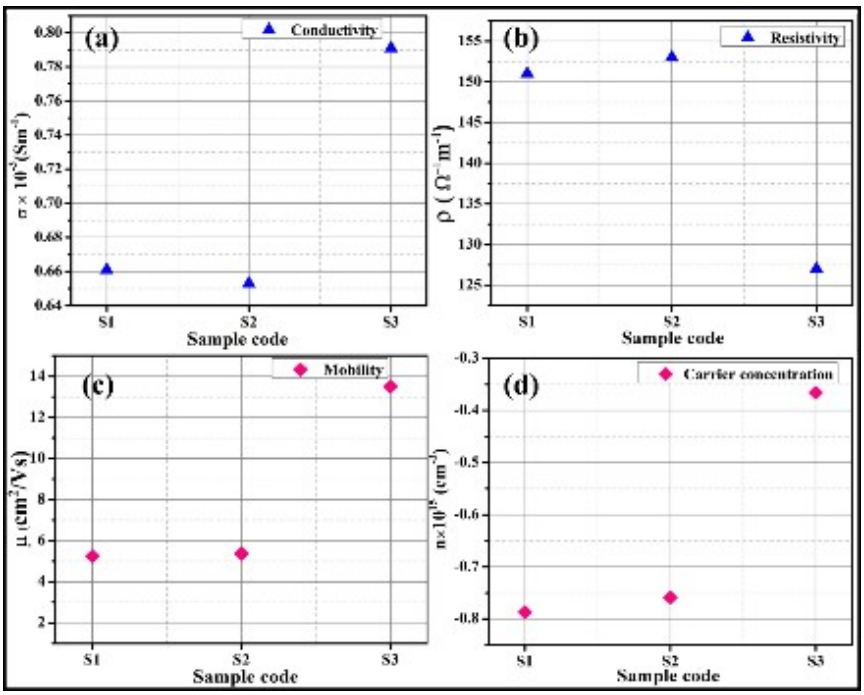

Fig. SP 3 Electrical conductivity, resistivity, mobility, and carrier concentration of BSb (a to d).

Polycrystalline BSb, consisting of many small crystals, have grain boundaries between them. These boundaries can impede electron flow, particularly if impurities or defects are concentrated at the boundaries. Adjusting the molar concentration can influence the grain size and boundary characteristics, which in turn can affect electrical conductivity[6]. The electrical resistivity shows a linear increase from S1 to S2, a trend typical of semiconductors, indicating that the BSb sample is degenerately doped with a high concentration of electrons. In contrast, the S3 sample shows a notably higher conductivity, consistent with its reduced resistivity. This decrease in resistivity, is due to combined influence of carrier concentration and mobility. The key relationship between carrier concentration and resistivity as the molar concentration increases, lies in the interplay between the rise in charge carriers and the reduction in their mobility due to enhanced scattering. As molar concentration increase, the reduction in mobility caused by scattering can surpass the impact of the higher carrier concentration, resulting in a net increase in resistivity[7].

Among the three BSb ratios studied, the S2 sample shows the lowest electrical conductivity. This reduction in conductivity is attributed to grain boundary effects and potential changes in stoichiometry, results in reduced thermal conductivity and an enhanced Seebeck coefficient compared to the other ratios. Fig. SP 3 (c & d) illustrates the mobility and carrier concentration values for the three BSb ratios. From Fig. SP 3 (c & d) we can observe that, S1 and S2 have comparable mobility values (~5 cm^2/Vs) whereas S3 shows a substantially higher value. This enhanced mobility at S3 suggests that the grain boundary scattering is less in S3 compared to S2 enabling carriers to freely move through the material. An optimal carrier concentration and mobility have been achieved for S2 among different BSb ratios due to the formation of additional grain boundaries that trap carriers, which is expected to positively influence its thermoelectric properties like seebeck coefficient. The measured BSb samples consistently showed negative carrier concentration values, confirming their behavior as n-type semiconductor.

Table 1: Hall measurement data for BSb.

Ratio	**Electrical conductivity (Sm^{-1})**	**Electrical resistivity ($\Omega^{-1}m^{-1}$)**	**Carrier concentration (cm^{-3})**	**Carrier type**	**Hall mobility (cm^2/Vs)**
S1	6.61×10^{-3}	1.51×10^{2}	7.87×10^{15}	N	5.24
S2	6.52×10^{-3}	1.53×10^{2}	7.59×10^{15}	N	5.37
S3	7.91×10^{-3}	1.27×10^{2}	3.66×10^{15}	N	13.5

7. Thermal conductivity and effusivity

In semiconductors, heat is primarily transmitted by phonons, which possess lower energy compared to electrons and are predominantly transmitted in highly degenerate semiconductors or metals. Thermal conductivity measures how effectively heat in the form of thermal energy in motion can pass through a material under a temperature gradient. The thermal conductivity of a solid comprises of two components, the vibrational (lattice) thermal conductivity and the electronic thermal conductivity, which results from the contribution of electrons. The Wiedemann−Franz law indicates an interdependent relationship between electrical conductivity and electronic thermal conductivity ($K_e = \sigma LT$, where L is the Lorenz

number). Therefore, it is reasonable to expect that the graphical trends of thermal conductivity (k_e) become similar to those of electrical conductivity (σ), shown in Fig. SP 4 (a). The following Fig. SP 4 (a & b) illustrates a graphical representation of the thermal conductivity versus temperature of BSb, in which there is a decrease in thermal conductivity at S2, followed by an increase at S3, with the lowest thermal conductivity of 0.059 W/mK and effusivity of 121.7 $Ws^{1/2}/m^2K$ observed at the S2 ratio of BSb. This occurrence could arise from significant phonon scattering observed at interfaces formed at higher mole ratios, such as S2. The underlying mechanism involves a partial hindrance in heat flow as it traverses these interfaces, leading to pronounced heat loss. This is primarily attributed to significant phonon scattering at the interfaces due to disparities in vibrational harmonics, acoustic characteristics, and modulus properties during the heat transfer process, resulting in a notable reduction in the mean free path of phonons[8].

Thermal effusivity is a measure of ability of a material to exchange thermal energy with its surroundings, combining the properties of thermal conductivity, density, and specific heat capacity to describe how readily a material can conduct and store heat. From the graph below in Fig. SP 4 (b), we can observe that the thermal effusivity of BSb has low effusivity at S2 (121.7 $Ws^{1/2}/m^2K$). Materials with low thermal effusivity exchange less heat with their surroundings. Typically, low thermal effusivity is associated with lower thermal conductivity. This reduced thermal conductivity limits the amount of heat that escapes from the hot side of the thermoelectric device, allowing the temperature gradient to be maintained more effectively and thus boosting the power output of the device.

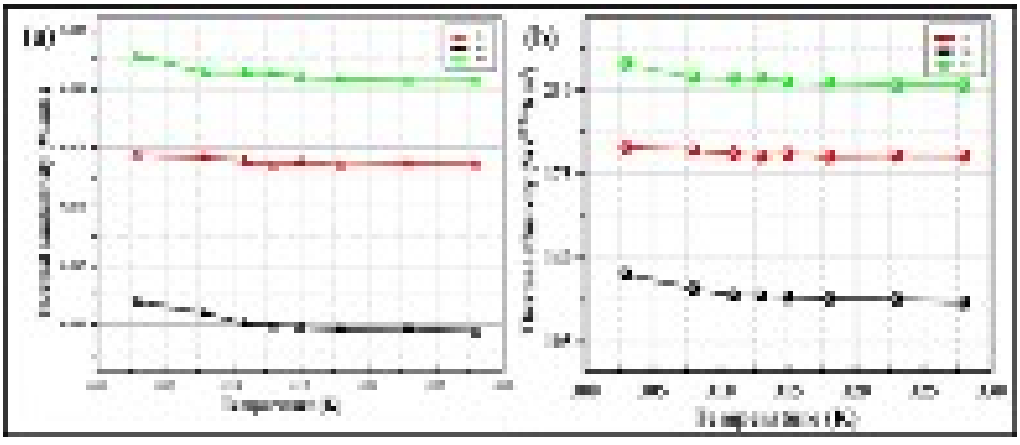

Fig. SP 4 (a) and (b) represent the thermal conductivity and thermal effusivity as a function of temperature for samples S1, S2, and S3.

8. References

1. Mani et al. Enhancing the Thermoelectric Performance of Cu2S/CuO Nanocomposites Through Energy-Filtering effect and Phonon Scattering. *J. Inorg. Organomet. Polym. Mater.* 2024, 34, 1548–1563.

2. Lincoln et al. A hybrid ceramic-based flexible thermoelectric nanogenerator with enhanced thermopower for human energy harvesting. *Energy Convers. Manage.* 2023, 292, 117364.

3. Mitra, S. S. Vibration Spectra of Solids, Phys. Status Solidi, 1962,13, 1-80.

4. Das et al. Synthesis and characterization of boron antimonide films by pulsed laser deposition technique. *Appl. Surf. Sci.* 2015, 353, 439–448.

5. Buciuman at al. Vibrational spectroscopy of bulk and supported manganese oxides. *PCCP.* 199, 1, 185–190.

6. Dolabella et al. Lattice Strain and Defects Analysis in Nanostructured Semiconductor Materials and Devices by High-Resolution X-Ray Diffraction: Theoretical and Practical Aspects. *Small Methods*., 2021, 6, 2100932.

7. Wu et al. Scattering Mechanisms and Compositional Optimization of High-Performance Elemental Te as a Thermoelectric Material. *Adv. Electron. Mater*. 2020, 6, 2000038.

8. Mehra et al. Thermal Transport in Polymeric Materials and across Composite Interfaces; *Appl. Mater. Today.* 2018, 12, 92-130.